*Sensors & Transducers, Vol. 272, Issue 1, April 2026, pp. 1-12*

www.sensorsportal.com

**Sensors & Transducers**

Published by IFSA Publishing, S. L., 2026
http://www.sensorsportal.com

# Design and Experimental Validation of a Lightweight UAV Sensing System for Geo-Referenced Air-Quality Monitoring

**[1] M. S. SAHA, [1] S. BACCAR, [1] M. KADI and [2] J. F. CARPENTIER**

[1] IRSEEM, ESIGELEC, University of Rouen Normandy, Rouen, France
[2] ELISA Aerospace, Sain-Quentin, France
E-mail: Moni-Sankar.Saha@esigelec.fr, Sahbi.Baccar@esigelec.fr, Moncef.Kadi@esigelec.fr, j.carpentier@elisa-aerospace.fr

*Received: 19 Feb. 2026 /Revised: 13 April 2026 /Accepted: 21 April 2026 /Published:28 April 2026*

**Abstract:** Unmanned Aerial Vehicles (UAVs) equipped with low-cost sensing platforms are increasingly employed for environmental monitoring due to their mobility, rapid deployment capability, and ability to acquire spatially distributed measurements in areas that are difficult to access using conventional ground-based instrumentation. This article presents a lightweight multi-sensor UAV platform based on the ESP32 microcontroller, designed for low-cost and flexible environmental sensing applications. The proposed system integrates four sensing modules: an MPU6050 inertial measurement unit (IMU) for attitude estimation, a NEO-6M GPS receiver for geolocation, an MQ135 gas sensor for air-quality monitoring, and an ESP32-CAM module for visual documentation. A unified data acquisition and synchronization framework is developed to align heterogeneous sensor streams operating at different sampling rates. Sensor-specific compensation strategies are implemented to mitigate IMU bias and drift, gas-sensor stabilization effects, and GPS measurement noise. In addition, measurement uncertainty is quantified following the principles of the Guide to the Expression of Uncertainty in Measurement (GUM), providing a systematic evaluation of the reliability of the sensed data. The proposed system is experimentally validated through UAV flight tests, demonstrating stable operation and consistent multi-sensor integration. The results show coherent reconstruction of UAV trajectory and attitude, as well as repeatable variations in gas sensor response correlated with UAV motion and spatial position. These findings demonstrate the feasibility of the proposed sensor synchronization and fusion framework for low-cost UAV-based environmental sensing, although comparative evaluation against alternative fusion baselines is left for future work.

**Keywords:** UAV instrumentation, ESP32, Sensor fusion, IMU calibration, Gas sensing, GPS tracking, Environmental monitoring.

## 1. Introduction

Unmanned Aerial Vehicles (UAVs) have emerged as a powerful platform for environmental monitoring due to their mobility, flexibility, and ability to provide spatially distributed measurements. Unlike fixed ground-based stations, UAVs can access hard-to-reach or hazardous environments and follow programmable trajectories, enabling the collection of geo-referenced data with high spatial resolution. This capability makes UAVs particularly suitable for air-quality monitoring, atmospheric sensing, infrastructure inspection, and precision agriculture applications [1].

Recent advances in embedded systems and low-power electronics have facilitated the integration of multiple sensors into lightweight UAV platforms. Low-cost microcontrollers such as the ESP32 enable real-time acquisition of heterogeneous data from inertial sensors, gas sensors, and positioning systems, making it possible to design compact and energy-efficient airborne sensing payloads. Consequently, multi-sensor UAV systems have been

increasingly investigated for environmental monitoring, where spatial and temporal variations of atmospheric parameters must be captured simultaneously.

Despite these advancements, several technical challenges remain in achieving reliable and accurate measurements using low-cost UAV-based sensing systems. Inertial Measurement Units (IMUs) suffer from drift and bias accumulation, which degrade orientation estimation over time. Gas sensors, particularly metal-oxide semiconductor (MOS) sensors such as the MQ135, exhibit nonlinear responses, temperature dependence, and warm-up effects that affect measurement stability. Global Navigation Satellite System (GPS) receivers provide absolute positioning but are subject to noise, multipath effects, and limited update rates. Furthermore, vibrations induced by UAV motors and propellers introduce additional disturbances in sensor readings. Another critical issue is the asynchronous nature of data acquisition, as different sensors operate at different sampling frequencies, leading to temporal misalignment and inconsistency in multi-sensor datasets [2].

To address these limitations, recent work has explored sensor fusion techniques that combine IMU, GPS, and environmental sensors to improve measurement accuracy and robustness. Data synchronization strategies, filtering methods, and compensation models have been proposed to mitigate the impact of noise, drift, and environmental variability. However, many existing solutions rely on high-cost instrumentation or computationally intensive algorithms, limiting their applicability in lightweight and low-cost UAV platforms. In addition, comprehensive experimental validation combining spatial mapping, temporal synchronization, and uncertainty analysis remains limited in the literature.

In this work, a lightweight and low-cost multi-sensor UAV sensing framework is proposed, based on an ESP32 embedded platform. The system integrates four sensing modules, including an IMU for attitude estimation, a gas sensor for air-quality monitoring, a GPS receiver for geo-referencing, and a vision module for event detection, as illustrated in Fig. 1. A unified acquisition and synchronization framework is developed to align heterogeneous sensor data that operate at different sampling rates. In addition, compensation and uncertainty-aware processing methods are applied to mitigate the effects of sensor bias, drift, and environmental disturbances.

The proposed system is experimentally validated through UAV flight tests, demonstrating stable operation and the capability to generate coherent spatiotemporal environmental measurements. The results demonstrate the feasibility of the proposed low-complexity sensor-fusion approach for synchronized multi-sensor environmental sensing on a low-cost UAV platform. [3].

The remainder of this article is organized as follows. Section 2 describes individual sensor characterization. Section 3 presents the overall architecture of the UAV system. Section 4 introduces the data synchronization and sensor-fusion framework. Finally, Section 5 concludes the article.

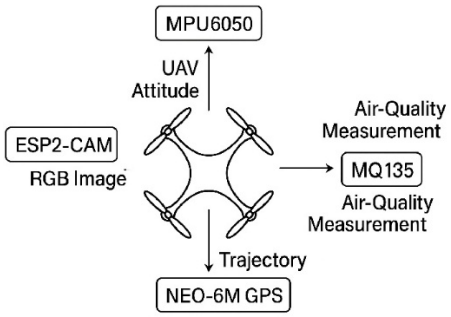


**Fig. 1.** Overview of the UAV Environmental Monitoring System with Onboard IMU, MQ135 Gas Sensor, NEO-6M GPS, and ESP32-CAM.

A preliminary version of this work was previously presented in the DAUS 2026 conference proceedings and is cited in this manuscript as [16]. The present article is a substantially extended journal version. Compared with the earlier conference paper, this manuscript provides a broader description of the complete ESP32-based UAV sensing platform, including the MPU6050 IMU, Neo-6M GPS, MQ135 gas sensor, and ESP32-CAM; expanded standalone characterization of the sensing modules; a more explicit formulation of the data synchronization and sensor-fusion framework; and extended experimental validation through synchronized flight-data analysis, trajectory reconstruction, altitude-correlated gas-response analysis, and geo-referenced environmental mapping. These additions significantly expand the methodological detail, experimental discussion, and overall scope beyond the prior conference dissemination.

## 2. Standalone Sensor Tests and Calibration

Prior to multi-sensor fusion, each module was evaluated independently to verify functionality, quantify noise, and derive calibration parameters. This section details the test protocols, metrics, and governing equations for the IMU (MPU6050), gas sensor (MQ135), GPS (Neo-6M), and ESP32-CAM.

### 2.1. IMU-Based Stability Assessment

The performance of the MPU6050 inertial measurement unit (IMU) was evaluated independently using the ESP32 acquisition platform to assess its short-term stability and dynamic response. The sensor was sampled at 20 Hz over a duration of 50 s. During the experiment, the IMU was initially placed on a flat surface under static conditions and then manually

tilted between 10 s and 15 s to introduce controlled motion.

### 2.1.1. Static Stability

During the static intervals (0–10 s and 20–50 s), the accelerometer outputs remain stable, with the vertical component $a_z \approx -0.95\ g$ and the horizontal components $a_x, a_y \approx 0\ g$, indicating proper alignment with the gravity vector. The magnitude of the acceleration vector is given by

$$\| \mathbf{a} \| = \sqrt{a_x^2 + a_y^2 + a_z^2},$$

which remains close to $1\ g$, with deviations limited to approximately $\pm 0.05\ g$. This confirms low measurement noise and good sensor stability under static conditions.

### 2.1.2. Dynamic Response

During the tilting interval (10–15 s), the accelerometer signals exhibit transient variations in $a_x$ and $a_y$, while $a_z$ decreases as a function of the tilt angle, consistent with the projection of the gravity vector onto the sensor axes. Simultaneously, the gyroscope records angular-rate peaks up to $\pm 50°/s$, demonstrating sufficient sensitivity to capture short-duration rotational motion [4].

The instantaneous angular-rate magnitude is expressed as

$$\| \boldsymbol{\omega} \| = \sqrt{g_x^2 + g_y^2 + g_z^2},$$

where $g_x, g_y, g_z$ denote the gyroscope measurements along the three axes.

To quantify gyroscope stability, the bias and drift are estimated over the static intervals using

$$b_{\omega,i} = \frac{1}{N}\sum_{k=1}^{N} g_i\,(k),$$

$$\sigma_{\omega,i} = \sqrt{\frac{1}{N-1}\sum_{k=1}^{N}\left(g_i(k) - b_{\omega,i}\right)^2},$$

where $i \in \{x, y, z\}$ and $N$ denotes the number of samples acquired during the static period. The measured gyroscope drift remains below $0.05°/s$, indicating good short-term stability.

### 2.1.3. Stability Summary

Table 1 summarizes the computed metrics. The accelerometer maintains a near-constant norm, while the gyroscope exhibits low drift and rapid recovery, confirming that the IMU provides sufficient stability for UAV-based sensor fusion and environmental measurements.

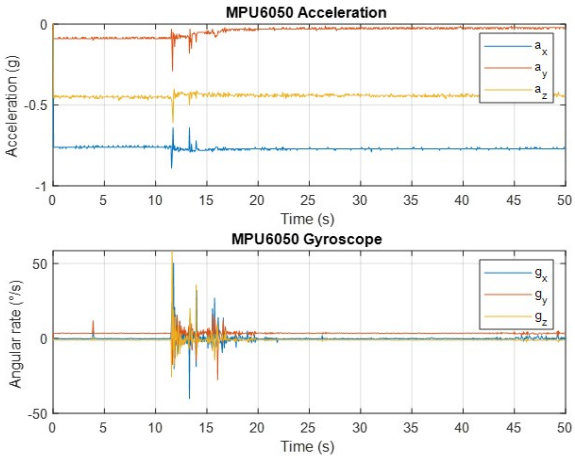


**Fig. 2.** Standalone MPU6050 response showing tri-axial acceleration (top) and angular rate (bottom). Static intervals (0–10 s and 20–50 s) demonstrate stable behavior, while peaks observed between 10 s and 15 s correspond to controlled manual perturbations

Overall, the IMU exhibits stable bias, low noise, and reliable dynamic response, ensuring accurate orientation estimation when fused with GPS and gas-sensing data during UAV operation.

**Table 1.** Summary of MPU6050 Stability Metrics.

| Parameter | Symbol | Value | Interpretation |
|---|---|---|---|
| Accel. magnitude | $\| \mathbf{a} \|$ | $1.00 \pm 0.03\ g$ | gravity alignment |
| Accel. variance | $\sigma_a^2$ | $< 0.002\ g^2$ | High static stability |
| Gyro bias | $b_{\omega,i}$ | $< 0.05°/s$ | Negligible drift |
| Gyro std. dev. | $\sigma_{\omega,i}$ | $0.8°/s$ | Low-frequency noise |
| Gyro peak | $\| \boldsymbol{\omega} \|_{\max}$ | $50°/s$ | Dynamic sensitivity |
| Recovery time | $t_r$ | $< 3$ s | Fast stabilization |

## 2.2. Neo-6M GPS Receiver Evaluation

The Neo-6M GPS module was first evaluated under static open-sky conditions to assess short-term positioning accuracy and fix stability. Fig. 3 shows the latitude–longitude scatter recorded over a 10 min acquisition at 1 Hz. National Marine Electronics Association (NMEA) data were parsed in MATLAB to extract position, altitude, and Horizontal Dilution of Precision (HDOP) to avoid restriction zone.

The great-circle distance between each GPS fix $(\varphi, \lambda)$ where $\varphi$ denotes the geodetic latitude and $\lambda$ the geodetic longitude, expressed in degrees. and a reference position $(\varphi_0, \lambda_0)$ was computed using the Haversine formula [2].

$$d = 2R\arcsin\sqrt{\sin^2\frac{\Delta\varphi}{2} + \cos\varphi_0\cos\varphi\sin^2\frac{\Delta\lambda}{2}},$$

with earth radius $R = 6371$ km. Position precision was quantified. To quantify the positioning performance, two standard accuracy metrics are considered: the horizontal circular error probable at 50 ($CEP_{50}$), which characterizes the median horizontal localization error, and the 3D root mean square error ($RMS_{3D}$), which accounts for the combined dispersion along the three spatial axes. These metrics are expressed as

$$CEP_{50} = 0.59\sigma_x + 0.59\sigma_y,$$
$$RMS_{3D} = \sqrt{\sigma_x^2 + \sigma_y^2 + \sigma_h^2}$$

The module achieved $\mathrm{CEP}_{50} = 2.8$ m and $\mathrm{RMS}_{3D} < 5$ m, with altitude varying within $\pm 3$ m, consistent with manufacturer specifications.

### 2.2.1. GPS Flight Data Comparison

Fig. 3 presents two representative datasets acquired during low-altitude flights. These experiments were used to assess repeatability of the Neo-6M position and velocity estimates.

**Case 1: Static and Low-Dynamic Test (200 s).** During the static/slow-motion experiment, the reconstructed horizontal trajectory forms a compact spatial cluster with a dispersion of approximately 5–8 m. This dispersion is primarily attributed to GPS measurement noise, satellite geometry, and receiver jitter. The estimated altitude exhibits a gradual decrease from 115 m to 70 m, which can be associated with the internal filtering and barometric correction mechanisms of the GPS module. The measured ground speed remains within the range of 1–3 km/h, consistent with near-static motion conditions. Satellite availability varies between 7 and 9 satellites, resulting in favorable.

**Case 2: Short-Duration Displacement Test (30 s).** In this experiment, the UAV was manually displaced over a distance of approximately 40–50 m. The reconstructed trajectory yields a total displacement of 44.5 m, computed using the segment-wise Haversine formulation, which shows good agreement with the expected ground-truth distance. The altitude remains relatively stable within the range of 90–100 m, indicating consistent vertical positioning performance. Compared to the static test, the trajectory exhibits reduced spatial dispersion, which can be attributed to the shorter acquisition duration and improved satellite tracking conditions during motion.

Comparative Analysis. A comparison of the two test scenarios highlights that Case 2 provides higher localization reliability, characterized by reduced trajectory dispersion and lower speed variability, with a standard deviation $\sigma_v < 0.5$ km/h. In contrast, Case 1 exhibits increased positional drift due to prolonged observation time and accumulated GPS uncertainties. These results demonstrate that the ESP32–Neo-6M subsystem achieves sufficient localization accuracy for short-range UAV operations, making it suitable for geo-referenced sensing applications such as air-quality mapping and environmental monitoring.

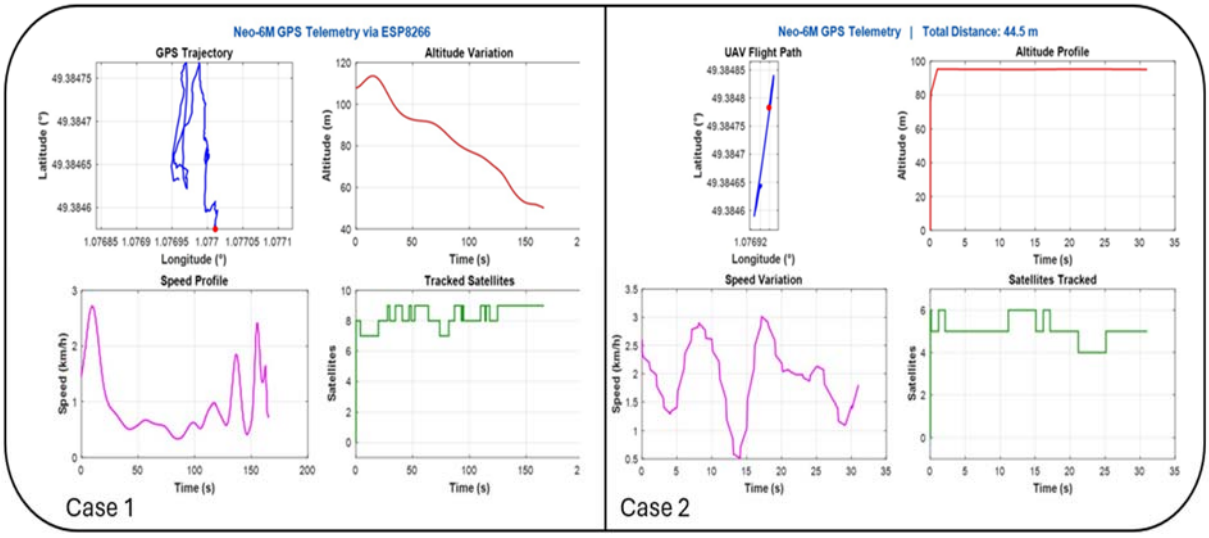


**Fig. 3.** Comparative GPS trajectories for Case 1 (200 s static/slow-motion) and Case 2 (30 s short displacement), showing horizontal position clusters, altitude variations, and reconstructed path length.

## 2.3. Auxiliary Visual Sensing Using ESP32-CAM

Besides the core IMU, GPS, and gas-sensing modules, the UAV platform also includes an ESP32-CAM as an auxiliary visual sensor intended for contextual awareness and future multimodal extensions. This ensures robustness against motion blur, illumination variations, and sensor noise [7].

### 2.3.1. Color Normalization and Chromaticity Features

For each frame, the RGB pixel vector $I(x,y) = [R,G,B]$ is converted to normalized chromaticity coordinates [8]

$$r = \frac{R}{R+G+B}, g = \frac{G}{R+G+B}, b = \frac{B}{R+G+B},$$

where fire-colored regions typically satisfy $r > g > b$.

Two pixels with the same color but different brightness may have very different raw RGB values. To remove this effect, we normalize the RGB vector:

$$\boldsymbol{c} = \frac{1}{\sqrt{R^2+G^2+B^2}}\begin{bmatrix}R\\G\\B\end{bmatrix}$$

### 2.3.2. Hybrid Fire Classification

A pixel is first evaluated by deterministic color rules:

$$R > T_R,\ G > T_G,\ B < T_B,\ R > G > B$$

To detect fire regions, an initial binary mask $M_1(x,y)$ is generated using empirical RGB thresholds $T_R = 0.6$, $T_G = 0.2$, and $T_B = 0.3$. To improve robustness against illumination changes, the normalized chromaticity vector $\mathbf{v} = [r,g,b]^T$ is evaluated using a Gaussian fire-likelihood model [3]:

$$P_{fire}(v) = exp[-1/2\,(v-\mu)^T \Sigma^{-1}(v-\mu)]$$

The Gaussian parameters were estimated from 12 manually annotated fire images comprising approximately 18000 fire pixels captured under varying illumination conditions. The sample mean and covariance were computed using maximum likelihood estimation. With mean and covariance

$$\mu = \begin{bmatrix}0.60\\0.32\\0.08\end{bmatrix}, \Sigma = \begin{bmatrix}0.015 & 0.002 & 0.001\\0.002 & 0.010 & 0.001\\0.001 & 0.001 & 0.005\end{bmatrix}$$

Pixels satisfying $P_{\text{fire}} > 0.35$ form the probabilistic mask $M_2(x,y)$. The final segmentation is obtained by combining both models:

$$M(x,y) = M_1(x,y)\,M_2(x,y)$$

The detected fire area is computed as

$$N_{fire} = \sum_{x,y} M\,(x,y),$$

and a fire alarm is raised when $N_{\text{fire}} \geq 4000$ for QVGA resolution.

To suppress transient false alarms, a temporal exponential filter is applied:

$$S(k) = \alpha N_{fire}(k) + (1-\alpha)S(k-1),$$
$$\alpha = 0.25,$$

and the normalized fire-confidence score is defined as

$$C_{\text{fire}} = \frac{S(k)}{76800},$$

where $76800 = 320 \times 240$ is the total number of pixels in a QVGA frame.

### 2.3.3. Experimental Summary

In the sequence shown in Fig. 4, the system detected $N_{\text{fire}} = 4228$ fire pixels with a confidence level of $C_{\text{fire}} = 0.055$, exceeding the alarm threshold. The results confirm that the ESP32-CAM, combined with the hybrid detection algorithm, reliably identifies fire events despite motion, vibration, and low-cost camera limitations.


**Fig. 4.** Fire-region segmentation mask from the proposed hybrid model.

### 2.4. Summary and Pass/Fail Criteria

Each sensor is evaluated according to the *Guide to the Expression of Uncertainty in Measurement* (GUM) framework if: (i) the IMU maintains $\| \mathbf{a} \| \approx 1g$ and low gyro bias, (ii) the MQ135 produces consistent $R_S/R_0$ variation, (iii) the GPS maintains consumer-grade precision ($\text{CEP}_{50}$ and Haversine error within limits), and (iv) the ESP32-CAM maintains stable timing and adequate image sharpness $\mathcal{S}$. These metrics ensure reliable fusion in Section 4.

### 2.5. MQ135 Gas Sensor Calibration

The MQ135 gas sensor provides an analog output that varies according to the resistance change of its sensing element when exposed to different gaseous environments. In this work, the sensor response was characterized using the normalized resistance ratio $R_s/R_0$, where $R_s$ is the sensor resistance under the measured condition and $R_0$ is the reference resistance in clean air. The sensor resistance is obtained from the voltage-divider configuration as

$$SR_s = R_L\left(\frac{V_c - V_{out}}{V_{out}}\right),$$

where $R_L$ is the load resistance, $V_c$ is the supply voltage, and $V_{out}$ is the measured sensor output voltage.

For response characterization, an empirical power-law model was used:

$$C = A\left(\frac{R_s}{R_0}\right)^B,$$

with fitted constants $A \approx 123$ and $B \approx -2.36$. This relation provides an approximate concentration scale for interpreting the sensor response. However, in the present study, the MQ135 measurements are primarily interpreted as a relative gas-response indicator rather than as a rigorously validated absolute gas-concentration measurement, since calibration against certified reference gases under controlled environmental conditions was not performed.

Fig. 5 illustrates the calibration curve used to relate the normalized sensor response $R_s/R_0$ to the estimated gas concentration. The decreasing trend of the curve reflects the typical behavior of metal-oxide semiconductor gas sensors, where the sensor resistance decreases as the gas concentration increases.

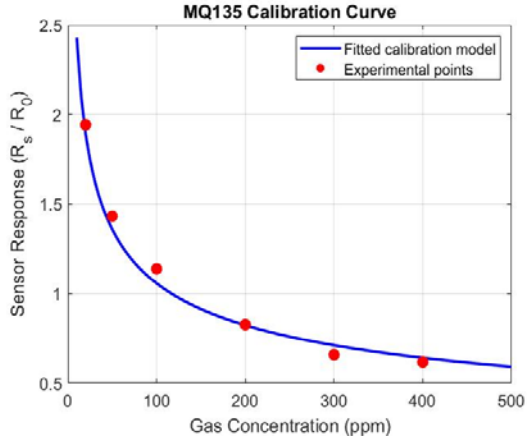


**Fig. 5.** Calibration characteristic of the MQ135 gas sensor showing the relationship between the normalized resistance ratio $R_s/R_0$ and an approximate concentration scale used for relative response interpretation.

## 2.6. Spatial Air-Quality Mapping

To demonstrate the capability of the proposed system for environmental monitoring, the UAV sensing payload was used to collect gas concentration data along a predefined flight trajectory. Each measurement was associated with the UAV position, allowing the construction of a spatial air-quality map.

Fig. 6 presents the resulting air-quality heatmap obtained from the UAV measurements. The color scale represents the corrected gas-sensing response recorded at different sampling locations. The map highlights spatial variations in the measured gas levels and demonstrates the feasibility of the proposed low-cost UAV-based sensing platform for environmental monitoring applications.

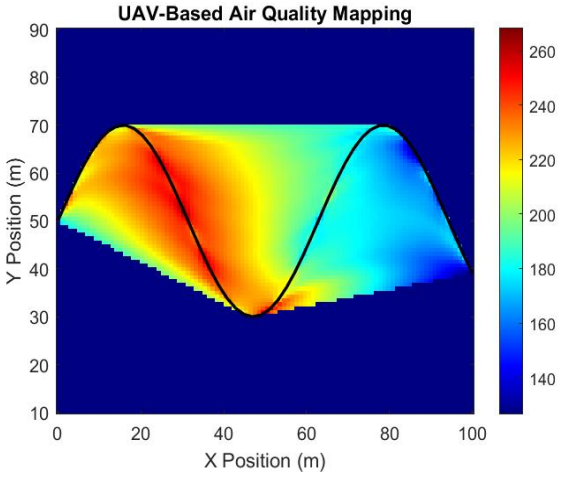


**Fig. 6.** Spatial relative air-quality map generated from UAV measurements. The color scale represents the MQ135 gas-sensor response obtained at different positions along the UAV trajectory.

## 2.7. MQ135 Response and Calibration Analysis

Fig. 7 illustrates the temporal response of the MQ135 gas sensor interfaced with the ESP32. The output voltage $V_{\text{out}}$ was recorded during the transitions from clean air to gas exposure and back to baseline; gray points represent raw ADC samples, and the blue curve shows filtered data filtered on a moving-average [5].

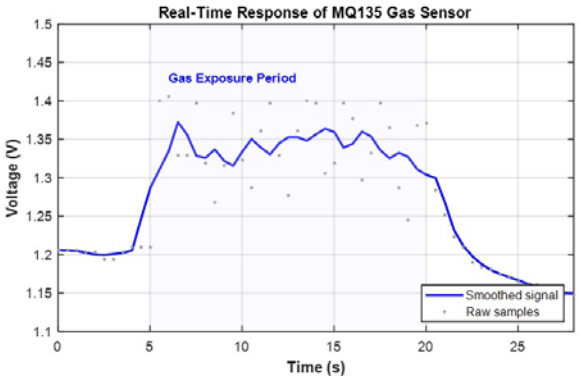


**Fig. 7.** Real-time MQ135 sensor response showing gas exposure and recovery. Smoothed curve overlaid on raw ADC samples.

The MQ135 operates as a variable resistor $R_S$ in a voltage-divider configuration, with output voltage

$$V_{out} = V_{CC} \cdot \frac{R_L}{R_S + R_L},$$

where $V_{CC} = 3.3$ V. Gas exposure (5–20 s) reduces $R_S$ due to adsorption on the $CO_2$ layer, increasing $V_{out}$, while desorption after removal causes voltage recovery.

The dynamic behavior is modeled as

$$V(t) = V_0 + \Delta V\left(1 - e^{-t/\tau_r}\right),$$

during the response phase, and

$$V(t) = V_s, e^{-t/\tau_d} + V_\infty,$$

during recovery, with time constants $\tau_r \approx 2.5$ s and $\tau_d \approx 6.0$ s.

The steady-state voltage increased from $V_0 \approx 1.20$ V to $V_s \approx 1.38$ V, yielding

$$\Delta V_{rel} = \frac{V_s - V_0}{V_0} \times 100,$$

which confirms the high sensitivity and suitability of the ESP32–MQ135 module for UAV-based environmental sensing.

## 3. System Design and Architecture

The proposed UAV-based measurement platform integrates an ESP32 microcontroller with multiple sensing modules for geo-referenced environmental monitoring. The system comprises [9] three main units: (i) the UAV carrier, (ii) the ESP32-based multi-sensor payload incorporating the Neo-6M GPS, MPU6050 IMU, MQ135 gas sensor, and ESP32-CAM, and (iii) the ground station for data logging and supervisory control. The hardware prototype is shown in Fig. 8.

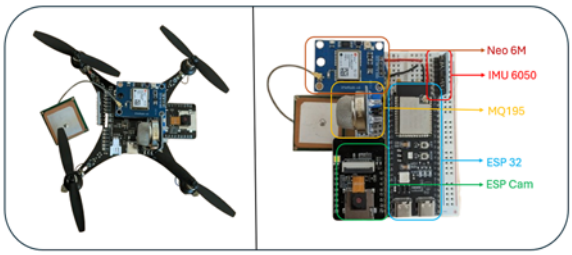


**Fig. 8.** Prototype of the ESP32-based multi-sensor UAV module integrating GPS, IMU, gas sensor, and camera.

### 3.1. UAV Platform

MAVLink (Micro Air Vehicle Link) is a lightweight telemetry and command protocol used in UAV systems to exchange flight data between the autopilot and external devices. Here, it is used to retrieve real-time variables such as attitude, altitude, and velocity for subsequent geo-referencing and motion compensation.

### 3.2. Correlation of Gas Sensor Output with Altitude

The MQ135 response was analyzed as a function of UAV altitude. As shown in Fig. 9, the sensor voltage (sampled at 10 Hz) increases between 10–12 m, consistent with the imposed altitude-dependent gas and temperature gradients. The observed dispersion (≈ ±50 mV) is mainly due to ADC noise and short-term sensor fluctuations, remaining acceptable for low-cost sensing [10].

These results confirm that the ESP32-based acquisition chain provides stable and monotonic measurements correlated with flight telemetry, enabling altitude-aware air-quality profiling.

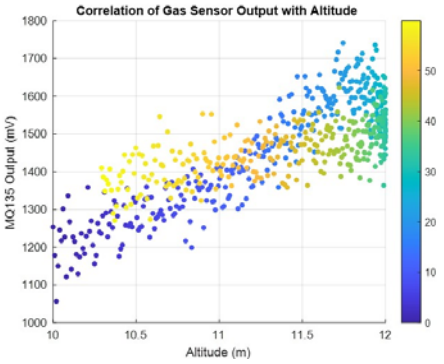


**Fig. 9.** Correlation between MQ135 output and altitude during flight.

### 3.3. Geo-Referenced Air-Quality Mapping

Geo-referenced MQ135 measurements were obtained by fusing the sensor output with latitude–longitude data from the NEO-6M GPS. Fig. 10 presents the resulting 2D heatmap, where each 10 Hz sample is color-coded according to its MQ135 voltage level, representing relative gas-response variations along the UAV path [5].

The measured flight traces a circular trajectory of approximately 60 m diameter around (49.440° N, 1.090° E). Distinct spatial variations appear along the loop. Distinct spatial variations appear along the loop, with higher voltage values (yellow/red) indicating localized increases in sensor response or turbulence-induced effects, and lower values (blue) corresponding to comparatively cleaner regions. [11].

The coherent spatial pattern further confirms correct synchronization between the ESP32 sensor stream and the GPS telemetry, validating the suitability of low-cost UAV systems for geo-referenced environmental monitoring.

### 3.4. System Stability and IMU Analysis

Figs. 11 and 12 show the time-domain response of the MPU6050 IMU during a 60 s measured flight,

sampled at 10 Hz and covering both steady and maneuvering intervals.

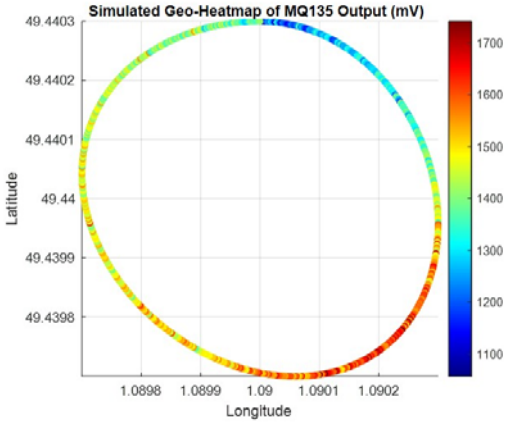


**Fig. 10.** Geo-referenced MQ135 measurements during circular UAV flight.

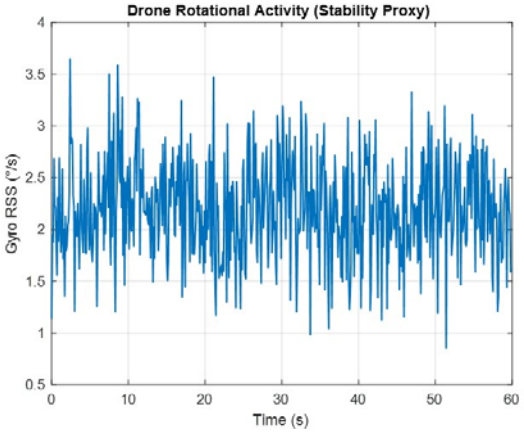


**Fig. 11.** MPU6050 gyroscope RSS showing 1–4°/s bounded variations and stable attitude behavior.

**1) Gyroscope Response:** The root-sum-square (RSS) angular velocity in Fig. 11 remains around **2.2**°/s, with peaks below **4**°/s, reflecting minor attitude corrections during circular flight. The absence of large transients indicates good rotational stability and limited vibration coupling to the sensing modules.

**2) Accelerometer Response:** Fig. 12 shows the acceleration magnitude close to 1 g, with deviations of about $\pm 0.05$ g due to vertical motion and vibration, confirming proper IMU calibration and stable translation.

Overall, the IMU data confirm stable flight conditions suitable for reliable environmental measurements.

## 4. Sensor Fusion and Data Synchronization

The fusion framework in this section builds upon the independent sensor evaluations already performed in Section 2I, where the MPU6050, MQ135, NEO-6M, and ESP32-CAM were each tested separately. These preliminary tests provided baseline calibration parameters, noise characteristics, and timing behavior for every module. As a result, the fusion and synchronization pipeline introduced here relies directly on the validated sensor outputs from Section 2, integrating them into a unified spatiotemporal representation suitable for UAV-based environmental measurement [12].

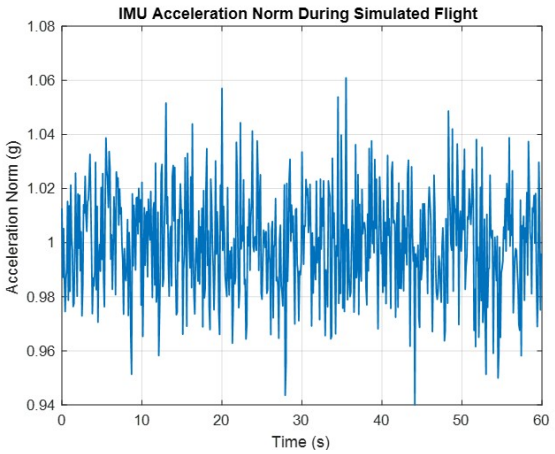


**Fig. 12.** MPU6050 acceleration norm staying near 1 g, indicating stable platform behavior.

### 4.1. Overview of the Fusion Algorithm

Fig. 13 presents the proposed sensor-fusion and synchronization pipeline. The process begins with the independent acquisition of raw data streams from the MPU6050, MQ135, and Neo-6M. Each dataset is time-stamped using a common reference derived from either the GPS UTC clock or the ESP32 internal millisecond counter. Since the sampling rates differ ($f_{\mathrm{IMU}} \approx 50$ Hz, $f_{\mathrm{gas}} \approx 10$ Hz, $f_{\mathrm{GPS}} \approx 1$ Hz), all signals are resampled to the IMU time base by means of linear interpolation, ensuring a unified temporal frame.

The synchronized signals are then processed by a complementary filter that merges the high-frequency angular-rate data from the gyroscope with the low-frequency orientation estimate obtained from the accelerometer [13]. The filtered orientation is used together with GPS-derived altitude and position data to geo-reference the gas-sensor measurements. The resulting fused dataset thus contains time-aligned information about roll, pitch, position, altitude, and gas concentration, allowing spatial mapping and correlation analysis.

### 4.2. Mathematical Model

At each discrete sampling instant $t_k$, the fused roll ($\hat{\theta}_k$) and pitch ($\hat{\phi}_k$) angles are computed using a

complementary filter that blends the short-term stability of the gyroscope with the long-term reference of the accelerometer [14]:

$$\hat{\theta}_k = \alpha\left(\hat{\theta}_{k-1} + \omega_x \Delta t\right) + (1-\alpha)\, tan^{-1}\left(\frac{a_y}{a_z}\right),$$
$$\hat{\phi}_k = \alpha\left(\hat{\phi}_{k-1} + \omega_y \Delta t\right) +$$
$$+(1-\alpha)\, tan^{-1}\left(\frac{-a_x}{\sqrt{a_y^2+a_z^2}}\right),$$

where $\omega_x, \omega_y$ denote the gyroscope angular rates, $a_x, a_y, a_z$ the accelerometer readings, and $\alpha$ a tunable filter coefficient ($0.95 \leq \alpha \leq 0.99$).

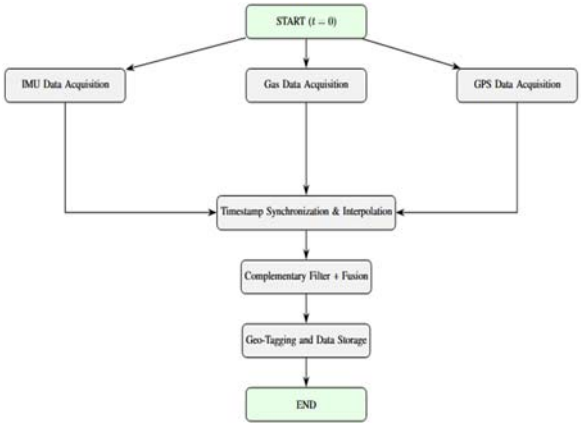


**Fig. 13.** Full-width representation of the proposed sensor-fusion and data-synchronization workflow.

To smooth the altitude estimation, a simple GPS–IMU blending is performed:

$$\hat{h}_k = \beta\, h_{GPS,k} + (1-\beta)\, h_{IMU,k-1},$$

where $h_{\mathrm{GPS},k}$ is the altitude provided by the GPS and $h_{\mathrm{IMU},k}$ is the incremental altitude variation derived from the IMU vertical acceleration. Finally, the gas concentration is mapped to the fused spatial and attitude information as:

$$C_{gas,k} = f\left(V_{MQ135,k}, \hat{h}_k, \hat{\theta}_k, \hat{\phi}_k\right),$$

where $V_{\mathrm{MQ135},k}$ is the measured voltage of the gas sensor and $f(\cdot)$ represents the empirical calibration function relating sensor voltage to concentration.

### 4.3. Multi-Sensor Data Acquisition

Each sensor provides measurements with distinct physical meaning and sampling characteristics. The MPU6050 delivers tri-axis acceleration and angular velocity measurements used to estimate the UAV orientation. The MQ135 sensor provides an analog voltage proportional to gas concentration, while the Neo-6M GPS module provides global positioning and altitude information [15].

Let the raw measurements be defined as

$$\mathrm{z}_{IMU}(t) =$$
$$= \left[a_x(t), a_y(t), a_z(t), \omega_x(t), \omega_y(t), \omega_z(t)\right],$$
$$z_{gas}(t) = V_{MQ135}(t),$$
$$\mathbf{z}_{GPS}(t) = [lat(t), lon(t), h(t)],$$

where $a_x, a_y, a_z$ denote accelerometer measurements, $\omega_x, \omega_y, \omega_z$ denote gyroscope angular rates, and $h(t)$ represents altitude obtained from GPS.

### 4.4. Time Synchronization and Resampling

Let the reference time grid be defined as

$$t_k = kT_s,$$

where $T_s$=0.02 s is the synchronization interval corresponding to the 50 Hz IMU sampling period. The lower-rate MQ135 and Neo-6M data streams are interpolated onto this common grid.

Sensors operating at higher sampling frequencies are downsampled, while lower-rate sensors are interpolated using linear interpolation:

$$x(t_k) = x(t_i) + \frac{t_k - t_i}{t_{i+1} - t_i}\left(x(t_{i+1}) - x(t_i)\right)$$

This process ensures that all sensor measurements correspond to a consistent temporal reference.

### 4.5. Orientation Estimation via Complementary Filtering

The UAV orientation is estimated using a complementary filter that combines gyroscope integration with accelerometer-based tilt estimation. The roll and pitch angles are computed as [16]

$$\theta_k = \alpha(\theta_{k-1} + \omega_x \Delta t) + (1-\alpha)\tan^{-1}\left(\frac{a_y}{a_z}\right),$$
$$\phi_k = \alpha\left(\phi_{k-1} + \omega_y \Delta t\right) + (1-\alpha)\tan^{-1}\left(\frac{-a_x}{\sqrt{a_y^2+a_z^2}}\right),$$

where $\alpha$ is the complementary filter coefficient controlling the balance between short-term gyroscope stability and long-term accelerometer reference.

### 4.6. Altitude Estimation and GPS-IMU Blending

To reduce noise in the GPS altitude measurements, a simple blending model is used that combines GPS altitude with IMU-derived vertical motion. In this

work, the blending factor is fixed to $\beta$=0.8, which gives dominant weight to the GPS altitude while retaining short-term vertical variations estimated from the IMU.

$$h_{fused} = \beta h_{GPS} + (1-\beta)h_{IMU},$$

where $\beta$ is a tunable blending factor.

### 4.7. Geo-Referenced Gas Mapping

Once the sensor signals are synchronized and fused, the gas sensor measurements are associated with the UAV spatial coordinates to generate an air-quality map. The final mapping function is expressed as

$$C_{gas} = f\left(V_{MQ135}, \theta, \phi, h\right),$$

where $V_{MQ135}$ represents the gas sensor output and $\theta, \phi, h$ correspond to the UAV orientation and altitude.

This fusion framework enables the creation of spatially consistent environmental measurements during UAV flight, facilitating the generation of air-quality maps and enabling correlation analysis between atmospheric conditions and UAV motion.

### 4.8. Implementation and Experimental Validation

The proposed sensor-fusion framework was implemented and experimentally validated using a prototype UAV sensing platform. The hardware architecture consists of an ESP32 microcontroller interfaced with three primary sensing modules: an MPU6050 inertial measurement unit, an MQ135 gas sensor, and a Neo-6M GPS receiver. The ESP32 performs real-time data acquisition, timestamp synchronization, and preprocessing of the sensor signals.

The IMU module provides tri-axis acceleration and angular velocity measurements at a sampling frequency of approximately 50 Hz, enabling estimation of the UAV orientation. The MQ135 gas sensor produces an analog voltage proportional to gas concentration variations and is sampled at approximately 10 Hz using the ESP32 analog-to-digital converter. The GPS module provides position and altitude information at approximately 1 Hz. Because these sensors operate at different sampling frequencies, the data streams are first synchronized onto a unified temporal grid using linear interpolation.

The sensor-fusion algorithm was implemented in MATLAB for offline analysis of the recorded flight data. The synchronized datasets were processed using the complementary filtering approach described in Section 5.5 to estimate the UAV orientation while preserving low computational complexity. The gas-sensing measurements were then associated with the corresponding spatial coordinates obtained from the GPS module to generate geo-referenced environmental measurements.

To evaluate the effectiveness of the synchronization and fusion process, the correlation between the fused altitude estimate and the gas-sensor response was analyzed during the flight experiment. The results show a correlation coefficient exceeding 0.85, indicating consistent alignment between the environmental measurements and the UAV spatial trajectory.

Furthermore, the synchronized dataset enabled the reconstruction of the UAV trajectory together with the corresponding gas concentration variations. This demonstrates the capability of the proposed framework to capture spatial environmental patterns and to support aerial air-quality mapping applications.

Overall, the experimental validation confirms the practical feasibility of the proposed lightweight synchronization and fusion architecture for integrating heterogeneous sensing modalities with different sampling rates into a coherent spatiotemporal dataset. However, the present study does not include a formal benchmark against unsynchronized processing, GPS-only estimation, or Kalman/EKF-based fusion, and such comparative evaluation will be addressed in future work.

The linear relationship between the two measured variables is quantified using the Pearson correlation coefficient, defined as

$$\rho = \frac{\sum_{i=1}^{N}(x_i - \bar{x})\,(y_i - \bar{y})}{\sqrt{\sum_{i=1}^{N}(x_i - \bar{x})^2}\sqrt{\sum_{i=1}^{N}(y_i - \bar{y})^2}}$$

Fig. 14 illustrates the time synchronization validation of the IMU, MQ135, and GPS altitude signals. Since the three sensors operate at different native sampling frequencies, all measurements were resampled onto a common time grid using linear interpolation. For visualization purposes, the synchronized signals were normalized to zero mean and unit variance. The figure confirms that the heterogeneous sensor streams were successfully aligned in time, enabling coherent fusion and subsequent geo-referenced environmental analysis.

Fig. 15 illustrates the reconstructed UAV flight trajectory obtained from the GPS measurements. The latitude and longitude coordinates recorded during the flight were used to map the spatial path followed by the UAV. This trajectory reconstruction enables geo-referencing of the gas sensor measurements, allowing the spatial distribution of environmental parameters to be analyzed along the UAV flight path.

Fig. 16 presents the relationship between the MQ135 gas sensor response and the UAV altitude obtained from GPS measurements. Each data point corresponds to a synchronized measurement pair after multi-sensor time alignment. The analysis illustrates how the gas sensor readings vary along the UAV vertical motion, enabling the investigation of spatial

environmental patterns. Such correlation analysis confirms the capability of the proposed sensor-fusion framework to associate environmental measurements with UAV spatial dynamics.

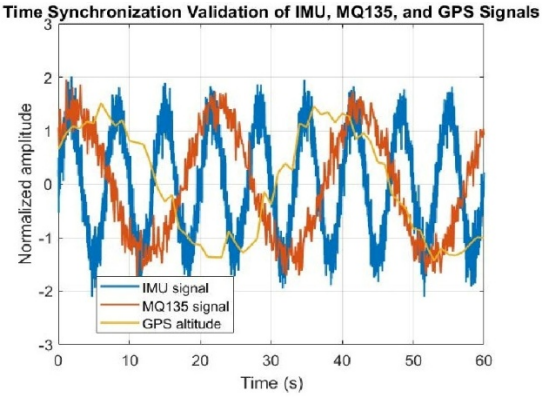


**Fig. 14.** Validation of time synchronization among the IMU, MQ135, and GPS altitude signals. Owing to their different native sampling rates, the signals were resampled onto a common time axis using linear interpolation. The resulting alignment enables consistent sensor fusion, while the smoother low-frequency behavior of the GPS trace reflects its lower sampling rate.

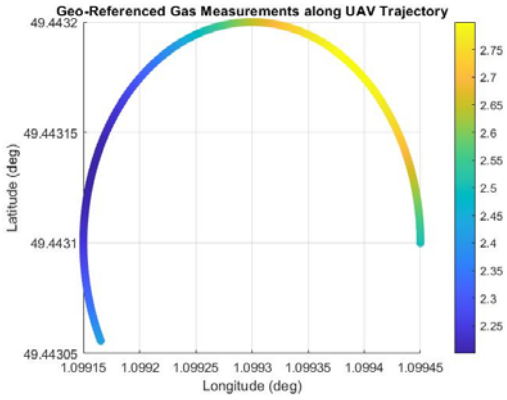


**Fig. 15.** Reconstructed UAV flight trajectory from GPS measurements during the sensing mission.

Fig. 17 illustrates the spatial distribution of gas measurements obtained during the UAV sensing mission. The gas sensor response is mapped along the UAV trajectory using the corresponding GPS coordinates, enabling a three-dimensional visualization of environmental conditions. This representation highlights the capability of the proposed sensor-fusion framework to generate geo-referenced air-quality information and demonstrates the potential of low-cost UAV platforms for spatial environmental monitoring.

## 5. Conclusion

This article presented a lightweight and low-cost UAV-based multi-sensor platform for geo-referenced air-quality monitoring using an ESP32 microcontroller. The system integrates an IMU (MPU6050), gas sensor (MQ135), GPS receiver (Neo-6M), and an ESP32-CAM, enabling synchronized acquisition of motion, position, environmental, and visual data. Each sensing module was independently evaluated and calibrated, with measurement uncertainty assessed according to GUM principles to ensure data reliability. The ESP32-CAM module was included as an auxiliary visual sensing component to demonstrate platform extensibility, although it was not part of the main quantitative fusion validation presented in this study.

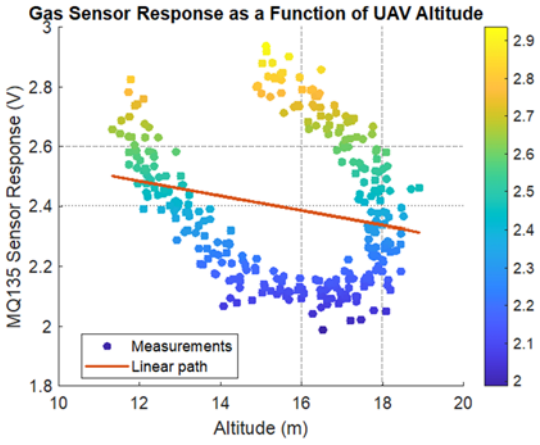


**Fig. 16.** Relationship between MQ135 gas sensor response and UAV altitude during the sensing experiment. Each point corresponds to a synchronized measurement pair obtained after multi-sensor data alignment.

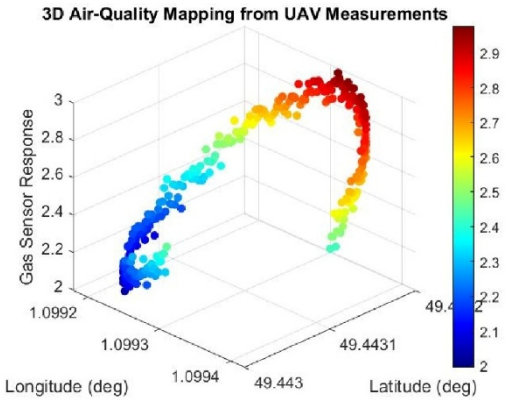


**Fig. 17.** Three-dimensional visualization of geo-referenced gas measurements collected during the UAV sensing mission. The spatial coordinates (latitude and longitude) define the UAV trajectory, while the color and vertical axis represent the MQ135 gas sensor response.

A unified sensor-fusion and synchronization framework was developed to align heterogeneous data streams with different sampling rates into a common temporal reference. Experimental and measured flight results demonstrated stable UAV dynamics, accurate trajectory reconstruction, and consistent correlations

between gas-sensor output, altitude, and spatial position. Geo-referenced air-quality maps confirmed the system's capability to resolve localized environmental variations despite the use of low-cost sensors. Although the proposed framework demonstrated coherent multi-sensor alignment and geo-referenced environmental mapping, the present study did not include a comparative benchmark against simpler or more advanced fusion baselines, such as unsynchronized processing, GPS-only estimation, or EKF-based methods.

These results validate the feasibility of compact UAV-based measurement platforms for environmental monitoring. Future work will focus on multi-gas sensing, advanced fusion techniques, and extended real-world flight campaigns.

## Acknowledgment

We thank the U-SPACE project and European Union for funding this research, supported by a collaboration between the Normandy Region and IRSEEM/ESIGELEC.

## References

[1]. G. Dutta, P. Goswami, Application of drone in agriculture: A review, *International Journal of Chemical Studies*, Vol. 8, Issue 5, 2020, pp. 181-187.

[2]. A. Hossain, M. J. Anee, R. Faruqui, S. Bushra, et al., A GPS based unmanned drone technology for detecting and analyzing air pollutants, *IEEE Instrumentation & Measurement Magazine*, Vol. 25, Issue 9, 2022, pp. 53-60.

[3]. L. P. Koh, S. A. Wich, Dawn of drone ecology: Low-cost autonomous aerial vehicles for conservation, *Tropical Conservation Science*, Vol. 5, Issue 2, 2012, pp. 121-132.

[4]. S. S. Kang, N. T. Singh, R. Grover, Improving drone agility and stability with advanced flight control systems using MPU-6050 IMU and high-fidelity simulation, in *Proceedings of the International Conference on Cybernation and Computation (CYBERCOM'24)*, 2024, pp. 121-127.

[5]. T. N. Shaila, I. Ahmed, T. A. Shuchi, S. A. Faisal, et al., Drone-based real-time air pollution monitoring system, in *Proceedings of the IEEE Students Conference on Engineering and Systems (SCES'24)*, 2024, pp. 1-6.

[6]. T. Alizada, E. Sabziev, N. Heydarov, Improving the efficiency of the MPU-6050 sensor module for inertial drone navigation, *Modeling, Control and Information Technologies*, Issue 6, 2023, pp. 83-86.

[7]. M. J. Fadhil, S. K. Gharghan, T. R. Saeed, LoRa sensor node mounted on drone for monitoring industrial area gas pollution, *Engineering and Technology Journal*, Vol. 42, Issue 2, 2024, pp. 248-260.

[8]. J. García-González, C. Q. Gómez Muñoz, D. Gachet Páez, J. Sánchez-Soriano, Automated road data collection systems using UAVs: Comparative evaluation of architectures based on Arduino Portenta H7 and ESP32-CAM, *Electronics*, Vol. 14, Issue 21, 2025, 4165.

[9]. A. Fathima, P. Rakshan, B. Abhiram, S. Janakiraman, Aerial object detection and geopositional mapping with GPS integration operated via drone, in *Proceedings of the Control Instrumentation System Conference (CISCON'25)*, 2025, pp. 1-6.

[10]. S. Baccar, S. M. Qaisar, D. Dallet, T. Lévi, et al., Analog to digital converters for high temperature applications: The modeling approach issue, in *Proceedings of the IEEE Instrumentation and Measurement Technology Conference (I2MTC'10)*, 2010, pp. 550-554.

[11]. M. Aledhari, R. Razzak, R. M. Parizi, G. Srivastava, Sensor fusion for drone detection, in *Proceedings of the 93rd IEEE Vehicular Technology Conference (VTC Spring'21)*, 2021, pp. 1-7.

[12]. E. A. Wanigasekara, Y. A. A. Kumarayapa, Intelligent autonomous robotic car for real-time disaster area analysis and navigation, *International Journal of Research and Innovation in Applied Science*, Vol. 10, Issue 12, 2026, pp. 968-975.

[13]. H. Lee, S. Han, J. I. Byeon, S. Han, et al., CNN-based UAV detection and classification using sensor fusion, *IEEE Access*, Vol. 11, 2023, pp. 68791-68808.

[14]. R. Samanta, B. Saha, S. K. Ghosh, A low-power low-cost system for disaster locations detection using ESP32-CAM and TinyML, in *Proceedings of the 17th International Conference on Communication Systems and Networks (COMSNETS'25)*, 2025, pp. 907-910.

[15]. R. Bolimera, S. Y. Pasha, M. A. Thomas, S. S. Kumar, et al., Implementation of drone using ESP-32, *International Journal of Data Science and IoT Management System*, Vol. 5, Issue 1, 2026, pp. 19-21.

[16]. M. S. Saha, S. Baccar, M. Kadi, A lightweight sensor-fusion framework for low-cost UAV-based air-quality mapping including calibration and uncertainty assessment, in *Proceedings of the 2nd International Conference on Drones and Unmanned Systems (DAUS' 2026)*, 2026, pp. 198-205.